Journal of Rock Mechanics and Geotechnical Engineering 16 (2024) 4004–4016

Contents lists available at ScienceDirect

Journal of Rock Mechanics and Geotechnical Engineering

journal homepage: www.jrmge.cn

Full Length Article

Study of hydro-mechanical behaviours of rough rock fracture with shear dilatancy and asperities using shear-flow model

Luyu Wang [a], Weizhong Chen [b,*], Qun Sui [b,c]

[a] Department of Civil and Environmental Engineering, The Hong Kong Polytechnic University, Hung Hom, Kowloon, Hong Kong, China
[b] Institute of Rock and Soil Mechanics, Chinese Academy of Sciences, Wuhan, 430071, China
[c] Changjiang Design Group Co., Ltd., Wuhan, 430010, China

ARTICLE INFO

Article history:
Received 12 August 2023
Received in revised form
1 November 2023
Accepted 20 November 2023
Available online 17 January 2024

Keywords:
Rock fracture
Stress-seepage coupling
Shear-flow model
Fracture asperity
Shear dilatancy

ABSTRACT

The geometric properties of fracture surfaces significantly influence shear-seepage in rock fractures, introducing complexities to fracture modelling. The present study focuses on the hydro-mechanical behaviours of rough rock fractures during shear-seepage processes to reveal how dilatancy and fracture asperities affect these phenomena. To achieve this, an improved shear-flow model (SFM) is proposed with the incorporation of dilatancy effect and asperities. In particular, shear dilatancy is accounted for in both the elastic and plastic stages, in contrast to some existing models that only consider it in the elastic stage. Depending on the computation approaches for the peak dilatancy angle, three different versions of the SFM are derived based on Mohr-Coulomb, joint roughness coefficient-joint compressive strength (*JRC-JCS*), and Grasselli's theories. Notably, this is a new attempt that utilizes Grasselli's model in shear-seepage analysis. An advanced parameter optimization method is introduced to accurately determine model parameters, addressing the issue of local optima inherent in some conventional methods. Then, model performance is evaluated against existing experimental results. The findings demonstrate that the SFM effectively reproduces the shear-seepage characteristics of rock fracture across a wide range of stress levels. Further sensitivity analysis reveals how dilatancy and asperity affect hydraulic properties. The relation between hydro-mechanical properties (dilatancy displacement and hydraulic conductivity) and asperity parameters is analysed. Several profound understandings of the shear-seepage process are obtained by exploring the phenomenon under various conditions.

1. Introduction

Fractures in natural rock formations are essential to various geological and engineering processes, such as groundwater flow, geological hazard assessment, energy exploration, and radioactive waste disposal (Wang et al., 2020; Zhang et al., 2022a; Zhou et al., 2023). The interaction between hydraulic and mechanical processes has received significant attention due to its profound impact on seepage pathways, hydraulic properties, and overall geomechanical responses (Dietrich et al., 2005; Kolditz et al., 2012; Tan et al., 2021). In this context, it is crucial to comprehend the hydro-mechanical characteristics of rough rock fractures to accurately model and predict subsurface fluid migration and deformation.

One fundamental aspect that governs the behaviour of rough rock fractures is the phenomenon of shear dilatancy (Segall and Simpson, 1986; Liu et al., 2023). Dilatancy describes the tendency of a rock fracture to widen when subjected to shear loading. This effect is particularly pronounced in fractures with irregular surfaces, often referred to as fracture asperities. These asperities are characterized by their roughness and local geometric features, serving as key factors in governing the contact behaviour of two sides of fracture surfaces (Zhang et al., 2022b; Gan et al., 2023). As shear stress is applied, these asperities interact in intricate ways, affecting the flow paths of fluids within the fractures (Lee and Cho, 2002; Sawayama et al., 2021; Jiang et al., 2022). The asperity-induced channels lead to preferential flow pathways, altering the transport properties of the fracture and influencing the overall seepage pattern.

* Corresponding author.
E-mail addresses: luyu.wang@polyu.edu.hk (L. Wang), wzchen@whrsm.ac.cn (W. Chen).

Peer review under responsibility of Institute of Rock and Soil Mechanics, Chinese Academy of Sciences.

https://doi.org/10.1016/j.jrmge.2023.11.020

To explore the phenomenon in depth, plenty of research studies are dedicated to the comprehensive analysis of the shear-seepage process within a single fracture. This phenomenon has been thoroughly investigated in the existing literature through laboratory tests, analytical models, and numerical simulations (Chen et al., 2021a, b; Jiang et al., 2022; Sui et al., 2022). As hydro-mechanical properties are inherent in the attributes arising from fracture asperities, the majority of researchers focus their attention on fracture roughness and asperity properties (Thompson and Brown, 1991; Cunningham et al., 2020; Liu et al., 2020). The coupling effect is primarily perceived to originate from mechanical to hydraulic effects. Consequently, in many engineering problems, the hydraulic process exerts minimal impact on the mechanical process, as indicated in several studies (Hudson et al., 2001; Chen et al., 2007; Zhou et al., 2023). Therefore, many researchers are interested in investigating the impact of mechanical effects on the evolution of hydraulic conductivity, particularly in the context of seepage flow in rock fractures (Chen et al., 2021a, b; Sui et al., 2022).

Numerous shear-flow models have been developed to comprehensively analyse the shear-seepage process. It focuses on accurately describing seepage through a single rock fracture. On one hand, a limitation arises from the inaccuracy of existing methods for parameter identification. This limitation results in reduced precision, primarily due to the issue of local optima (Sun et al., 2019). On the other hand, some models proposed in the early stages often oversimplify fracture surfaces as smooth, whereas real fractures are featured with roughness, asperities, and irregularities. Barton and Bandis (1980) introduced the concept of joint roughness coefficient (*JRC*) to quantify fracture roughness. This concept plays a pivotal role in understanding fracture mechanical properties and holds significant relevance in geomechanics (Kim et al., 2013; Liu et al., 2017; Barton et al., 2023). Some researchers have pointed out a limitation in the *JRC*-based model, caused by the inadequacy in representing the geometric anisotropic features (Grasselli et al., 2002; Tang et al., 2021). To tackle this concern, Grasselli et al. (2002) introduced an improved approach that integrates the effect of fracture asperities through the concepts of the maximum contact area and the maximum apparent dip angle (Grasselli et al., 2002; Grasselli and Egger, 2003). Subsequently, many authors have developed a range of models building upon Grasselli's approach (Tatone and Grasselli, 2009; Xia et al., 2014).

The present study explores the hydro-mechanical characteristics of rough rock fractures during shear-seepage processes. The primary focus lies in comprehending how dilatancy and fracture asperities collectively govern the coupled behaviours of seepage and mechanical deformation within fractures. By investigating these phenomena across a range of stress levels and different fracture patterns, a deeper insight into the shear-seepage process within rock fractures is attained.

The article is organized as follows. In Section 2, an improved shear-flow model is proposed with consideration of the effect of dilatancy and asperity. In Section 3, we present a method for determining parameters and an advanced optimization approach designed to accurately identify model parameters. In Section 4, descriptions of the shear-seepage experiment and the data source are provided. In Section 5, the proposed model is employed to reproduce the experimental results under different conditions with varying fracture asperities. A series of tests are conducted to thoroughly explore the effects of dilatancy and asperity on hydraulic conductivity.

2. An improved shear-flow model with dilatancy and asperity

In this section, we present a shear-flow model that incorporates essential components, including stress-dependent hydraulic conductivity, fracture closure, and asperity-induced dilatancy. Then, various versions of the proposed model are derived based on different theories.

2.1. Stress-dependent hydraulic conductivity

The hydraulic conductivity K_f (or permeability k_f) of rock fractures is significantly influenced by the stress state and the geometric features of fracture surfaces (Cunningham et al., 2020; Li et al., 2023). As illustrated in Fig. 1, the stress components acting in the normal and shear directions to the fracture are denoted as σ_n and τ. The geometric attributes and the mechanical strength of fracture are denoted as λ_1 and λ_2. Therefore, a general formula of the shear-flow model can be expressed as

$$K_f = K_f(\sigma_n, \tau, \lambda_1, \lambda_2) \tag{1a}$$

$$K_f = \frac{g}{\nu} k_f = \frac{\rho g}{\mu} k_f \tag{1b}$$

where g is the gravitational acceleration; ρ is the density of fluid; ν and μ are the kinematic viscosity and dynamic viscosity coefficients, respectively.

The primary objective of the present investigation is to formulate an explicit expression of Eq. (1), establishing a connection between stress, fracture asperity, and K_f. The cubic law provides a significant relation between the hydraulic conductivity K_f and the hydraulic aperture e_h (Dietrich et al., 2005; Zhou et al., 2023):

$$K_f = \frac{e_h^2 g}{12\nu} = \frac{e_h^2 g \rho}{12\mu} \tag{2a}$$

$$k_f = \frac{e_h^2}{12} \tag{2b}$$

As illustrated in Fig. 1b, the hydraulic aperture e_h is determined by the deformation of the fracture under shear-seepage conditions, particularly the displacement component normal to the fracture, represented as u_n. Normally, the magnitude of the hydraulic aperture is smaller than or equal to the initial mechanical aperture e_0, as the shear-seepage process tends to decrease the fracture aperture.

Several models exist for the determination of e_h. However, they are often hindered by the requirement of numerous uncertain coefficients, for example, Louis model (Louis, 1974), Matsuki model (Matsuki et al., 1999), and Rasouli-Hosseinian model (Rasouli and Hosseinian, 2011). To obtain parameters, substantial effort is required to acquire the geometric details of the fracture surface. Witherspoon et al. (1980) proposed a concise formula to calculate e_h:

$$e_h = e_0 - c_f u_n \tag{3}$$

where the dimensionless coefficient c_f ranges from 0.5 to 1. In modelling, it can be determined through the least square fitting, parameter optimization, or by using a direct predefined value. Consequently, Eq. (2) is further expressed as

$$K_f = \frac{g}{12\nu}\left(e_0 - c_f u_n\right)^2 \tag{4}$$

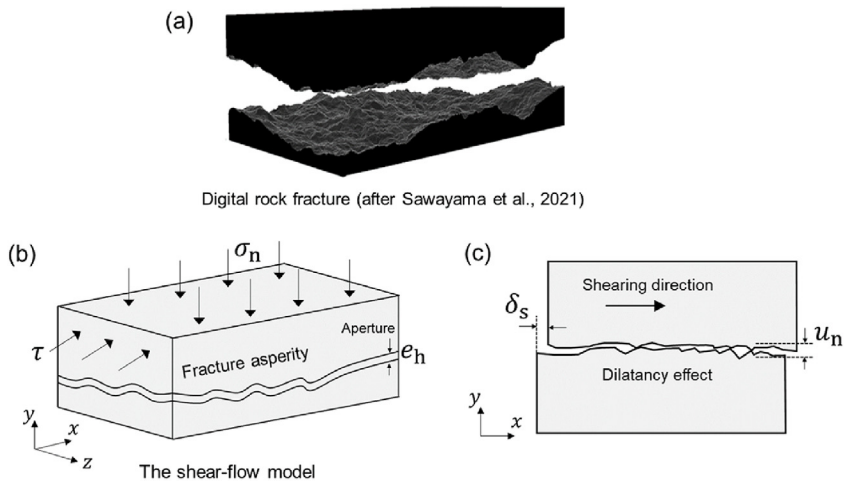

Fig. 1. Schematic of a rough rock fracture: (a) A digital image of a rough fracture (Sawayama et al., 2021), (b) The shear-flow model, and (c) Displacement components in the normal and shear directions along the fracture.

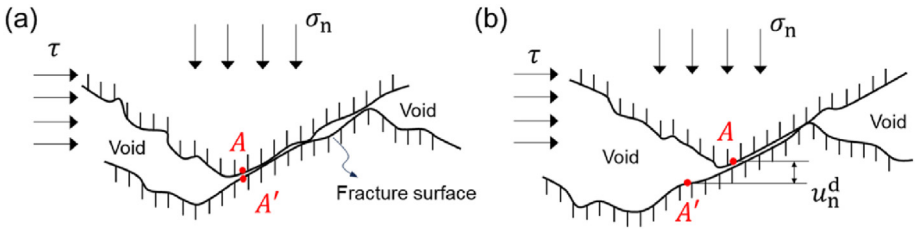

Fig. 2. Dilatancy-induced deformation during shear loading: (a) The initial state of rock fracture before shear loading, and (b) Dilatancy effect due to fracture asperities. A pair of contact points is denoted as A and A'.

2.2. Fracture closure

The initial mechanical aperture e_0 of a rough fracture can be predicted in the following expression (Bisdom et al., 2016; Barton et al., 2023):

$$e_0 = \frac{JRC}{5}\left(\frac{0.2\sigma_c}{JCS} - 0.1\right) \tag{5}$$

where JRC is the joint roughness coefficient (Barton, 2014); JCS is the joint compressive strength; and σ_c is the uniaxial compressive strength. σ_c equals to JCS if the rock fracture is unweathered.

As shown in Fig. 1c, the variable u_n in Eq. (4) consists of two parts of deformation, including the compressive-induced deformation Δu and the dilatancy-induced deformation u_n^d:

$$u_n = \Delta u + u_n^d \tag{6}$$

where Δu can be directly determined by the Barton–Bandis law (Barton and Bandis, 1980; Barton et al., 1985). The closure of fractures under the compressive stress σ_n is determined by a nonlinear hyperbolic function:

$$\Delta u = \left(\frac{1}{u_m} + \frac{K_{n0}}{\sigma_n}\right)^{-1} \tag{7}$$

where the initial normal stiffness K_{n0} and the maximum closure of fracture u_m are expressed as (Barton, 2014; Bisdom et al., 2016)

$$K_{n0} = -7.15 + 1.75JRC + 0.02\frac{JCS}{e_0} \tag{8a}$$

$$u_m = -0.1032 - 0.0074JRC + 1.135\left(\frac{JCS}{e_0}\right)^{-0.251} \tag{8b}$$

2.3. Dilatancy effect during shear loading

The dilatancy-induced deformation u_n^d in Eq. (4) is related to the shear displacement δ_s along tangential direction to the fracture. As shown in Fig. 2, the mismatching existing between the two surfaces results in significant relative movement between the asperities.

In the present model, we assume that the shear displacement δ_s consists of two parts:

$$\delta_s = \delta_s^e + \delta_s^p \tag{9}$$

where δ_s^e and δ_s^p are the shear displacements in elastic and plastic stages, respectively. The elastic part δ_s^e can be directly determined by

$$\delta_s^e = \tau / K_{s0} \tag{10}$$

where K_{s0} is the initial shear stiffness and can be obtained from experimental data; and τ is the shear stress.

As shown in Fig. 3a, once the deformation enters the plastic stage, the elastic deformation reaches its maximum value, given by

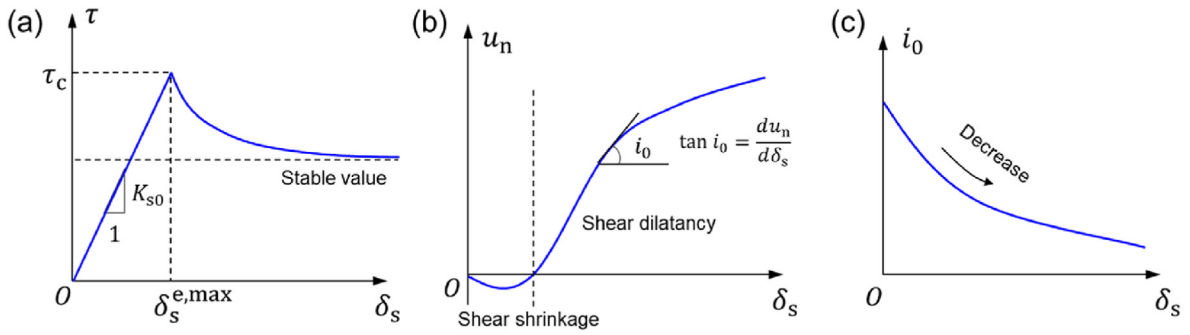

Fig. 3. Characteristics of rock fracture deformation during shear loading: (a) δ_s-τ curve and definition of K_{s0}, (b) δ_s-u_n curve and definition of i_0 in shear dilatancy, and (c) δ_s-i_0 curve.

$$\delta_s^{e,max} = \tau_c / K_{s0} \tag{11}$$

where τ_c represents the shear strength of fracture.

Assuming the dilatancy effect occurs in both the elastic and plastic stages, we formulate the dilatancy-induced displacement as follows:

$$u_n^d = s_f \left(\int_0^{\delta_s^e} \tan i_0 \mathrm{d}\delta_s^e + \int_0^{\delta_s^p} \tan i_0 \mathrm{d}\delta_s^p \right) \tag{12}$$

where s_f is a dimensionless coefficient with a range of 0–1; and i_0 is the dilatancy angle of fracture as described in Fig. 3b and c. It can be expressed as an exponential function of shear displacement (Barton and Bandis, 1982; Chen et al., 2007):

$$i_0 = i_{p0} \mathrm{e}^{-r_f \delta_s^p} \tag{13}$$

where i_{p0} is the peak dilatancy angle of fracture; $\mathrm{e}^{-r_f \delta_s^p}$ is an exponential function; and r_f is a positive coefficient. We expand the function tan i_0 using the Taylor series, that is tan $i_0 \approx i_0$. Eq. (12) is rewritten as

$$u_n^d = \int_0^{\delta_s^e} s_f i_0 \mathrm{d}(\delta_s - \delta_s^p) + \int_0^{\delta_s^p} s_f i_0 \mathrm{d}\delta_s^p = s_f \frac{i_{p0}}{r_f} \left(2 - \mathrm{e}^{-r_f \delta_s^e} - \mathrm{e}^{-r_f \delta_s^p} \right) \tag{14}$$

The peak dilatancy angle i_{p0} has a considerable effect on the dilatancy-induced deformation. Numerous studies suggest that i_{p0} depends on the properties of fracture asperity and mechanical strength. Different calculation methods of i_{p0} lead to various forms of the shear-flow model, as discussed in Section 2.5.

2.4. The asperity-induced dilatancy angle

The Mohr-Coulomb (MC) criterion predicts the shear strength of rock fracture (Jaeger et al., 2009):

$$\tau_c = \sigma_n \tan(\phi_b + i_{p0}) \tag{15}$$

where ϕ_b is the basic frictional angle. Therefore, the peak dilatancy angle i_{p0} can be directly derived:

$$i_{p0} = \arctan\left(\frac{\tau_c}{\sigma_n}\right) - \phi_b \tag{16}$$

where ϕ_b and τ_c can be obtained from the direct shear test.

Alternatively, a commonly used method for determining i_{p0} is based on the *JRC-JCS* criterion (Barton et al., 1985; Liu et al., 2017):

$$i_{p0} = JRC \log_{10}\left(\frac{JCS}{\sigma_n}\right) \tag{17}$$

Correspondingly, the *JRC-JCS* criterion can be analogously formulated to the MC criterion:

$$\tau_c = \sigma_n \tan\left[\phi_b + JRC \log_{10}\left(\frac{JCS}{\sigma_n}\right)\right] \tag{18}$$

However, some researchers have pointed out that the *JRC-JCS* criterion cannot effectively capture the geometric anisotropic property of rough fractures, due to insufficient information regarding the spatial asperity on fracture surfaces (Grasselli et al., 2002; Tang et al., 2021). To address this issue, Grasselli proposed a model that incorporates the effect of spatial asperity (Grasselli et al., 2002; Grasselli and Egger, 2003), considering the detailed geometric information of the rough fracture.

The shear dilatancy is influenced by the apparent dip angle θ^* rather than the geometric dip angle θ, as illustrated in Fig. 4. θ^* is calculated by (Grasselli et al., 2002):

$$\tan\theta^* = -\tan\theta\cos\alpha \tag{19}$$

where α is the azimuth. In Fig. 4, $\boldsymbol{n}_0$ is the unit vector normal to the shear plane; $\boldsymbol{n}_a$ is the unit normal vector of the fracture asperity; and $\boldsymbol{n}_1$ is the projection of $\boldsymbol{n}_a$ onto the shear plane.

In a shear loading process, the potential contact area A_{θ^*} represents the geometric intricacies of the fracture surfaces, as shown in Fig. 5. It can be expressed as a function of the apparent dip angle θ^* introduced in Eq. (19):

$$A_{\theta^*} = A_0 \left(\frac{\theta_{max}^* - \theta^*}{\theta_{max}^*}\right)^C \tag{20}$$

where A_0 and θ_{max}^* are the maximum possible contact area and the maximum apparent dip angle in the shear direction; and C is a coefficient and calculated by parameter optimization or curve fitting. Note that A_0 is a dimensionless quantity as indicted by Grasselli et al. (2002). Tatone and Grasselli (2009) derived the integral of A_{θ^*} as follows:

$$\int_0^{\theta_{max}^*} A_0 \left(\frac{\theta_{max}^* - \theta^*}{\theta_{max}^*}\right)^C \mathrm{d}\theta^* = A_0 \frac{\theta_{max}^*}{C+1} \tag{21}$$

where A_0 is almost constant ($A_0 = 0.5$) in many tests, as reported in literature (Liu et al., 2017). The term $\theta_{max}^*/(C+1)$ is regarded as a

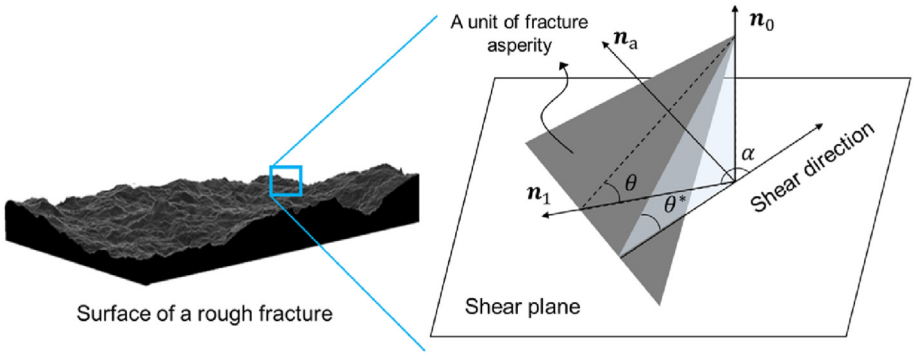

Fig. 4. Schematic of dilatancy when shear loading is applied on a unit of the fracture asperity.

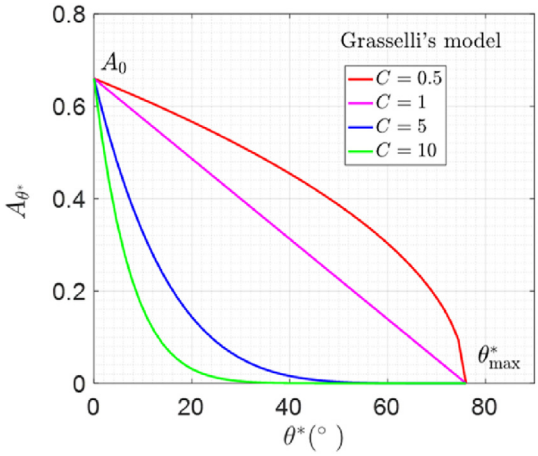

Fig. 5. The relation between θ^* and A_{θ^*} in Grasselli's model.

novel index for evaluating fracture roughness (Tatone and Grasselli, 2009; Barton et al., 2023).

Then, based on Grasselli's model, Xia et al. (2014) proposed a method for accurately calculating i_{p0}:

$$i_{p0} = 4A_0\frac{\theta^*_{max}}{C+1}\left[1+\exp\left(-\frac{1}{9A_0}\frac{\theta^*_{max}}{C+1}\frac{\sigma_n}{\sigma_t}\right)\right] \tag{22}$$

where σ_t is the tensile strength. Based on the results, Grasselli's model was extended to determine the shear strength:

$$\tau_c = \sigma_n \tan\left\{\phi_b + 4A_0\frac{\theta^*_{max}}{C+1}\left[1+\exp\left(-\frac{1}{9A_0}\frac{\theta^*_{max}}{C+1}\frac{\sigma_n}{\sigma_t}\right)\right]\right\} \tag{23}$$

Compared to the MC-based method and the *JRC-JCS*-based method, Grasselli's model takes into account the intricate details of fracture asperity. In Section 5, we will compare the differences among various calculation methods of i_{p0}.

2.5. Various forms of the proposed shear-flow model

The shear-flow model (Eq. (4)) can be expressed in various forms, depending on different calculation methods for the following aspects: (1) shear strength τ_c, and (2) the peak dilatancy angle i_{p0}. In the present study, we focus on three versions of the proposed model. The MC-based method employs Eqs. (15) and (16) to determine τ_c and i_{p0}, whereas the *JRC-JCS*-based method utilizes Eqs. (17) and (18) for the calculation.

One of the novelties of the proposed model is the integration of asperity-induced dilatancy via Eq. (14). Furthermore, our model incorporates the effect of fracture asperity based on Grasselli's approach using Eqs. (22) and (23). While commonly employed in purely mechanical processes of shear strength analysis, this method is seldom utilized for exploring the hydro-mechanical characteristics of rock fractures.

3. Model parameters: determination and optimization method

The shear-flow model proposed in Section 2 involves numerous parameters that require determination. In this section, we provide a method for determining model parameters and introduce an advanced optimization approach.

3.1. Determination of parameters in the shear-flow model

The proposed shear-flow model (SFM) has three different versions, as discussed in Section 2.5, including the MC-based method, *JRC-JCS*-based method, and Grasselli's method. In short, they are referred to as SFM-MC, SFM-*JRC*, and SFM-Grasselli, respectively. The parameters that need to be determined vary with each method. Table 1 provides all the parameters involved in the proposed model in various versions. The SFM-Grasselli excels in capturing intricate geometric details of rough fractures. This advantage comes at the cost of having a higher number of parameters when compared to the other two methods.

In the analysis, the ideal scenario is to obtain all parameters from experiments, ensuring their reliability and accuracy. However,

Table 1
Parameters of the proposed model in various versions.

Method	Experimental data	Uncertain parameters	Number of total parameters	Number of uncertain parameters
SFM-MC	*JRC*, *JCS*, σ_c, K_{s0}, τ_c, ϕ_b	c_f, r_f, s_f	9	3
SFM-*JRC*	*JRC*, *JCS*, σ_c, K_{s0}, ϕ_b	c_f, r_f, s_f	8	3
SFM-Grasselli	*JRC*, *JCS*, σ_c, K_{s0}, ϕ_b, A_0, θ^*_{max}, σ_t	c_f, r_f, s_f, C	12	4

Remarks: (1) Experimental data: the parameters can be obtained from experiments. (2) Uncertain parameters: the parameters cannot be obtained from experiments. (3) g, ρ and μ are constants set to 9.8 m/s^2, 1000 kg/m^3 and 8.9 $\times 10^{-4}$ Pa s, respectively.

in most scenarios, some parameters cannot be directly acquired from experimental data, for instance, c_f and r_f. The following key points are listed for determining parameters:

- K_{s0}, τ_c, and ϕ_b can be obtained from the direct shear test.
- *JCS* equals to σ_c for unweathered rocks as pointed out in literature (Olsson and Barton, 2001). σ_c can be obtained from the uniaxial compression test.
- σ_t can be predicted using the Brazilian split method or estimated through the empirical relation with σ_c.
- A_0, θ^*_{max} and *JRC* can be obtained through topography analysis of the rock fracture. However, sometimes experimental conditions may not allow for such tests. In this context, *JRC* can be predicted using the fracture profiles proposed by Barton et al. (2023).
- If one wishes to use SFM-Grasselli but lacks sufficient experimental data, A_0 and θ^*_{max} should be determined by parameter optimization.
- s_f, c_f, r_f and C are coefficients that need to be determined through curve fitting or parameter optimization, since they do not possess physical meanings compared to other mechanical parameters.

3.2. PSO-WDV method for parameter optimization

Parameter optimization enables the determination of uncertain parameters in scenarios where experimental data is limited. Classical least square-based fitting methods may encounter unexpected issues, making them susceptible to getting trapped in the dilemma of local optima (Sun et al., 2019; Tan et al., 2023).

To overcome this limitation, we integrate the particle swarm optimization with weighted delay velocity (PSO-WDV) into the proposed SFM. The PSO-WDV is an innovative parameter optimization method that extends the classical PSO (CPSO) with notable enhancements (Song et al., 2021; Xu et al., 2021). While it originated in the field of intelligent optimization, it has not yet been applied to geomechanics problems.

The objective function used in parameter optimization is as follows:

$$\min \phi(\boldsymbol{X}) = \sum_{i=1}^{N_d} \left\| K_{f,i} - \overline{K}_{f,i} \right\|_2 \tag{24}$$

where N_d is the number of data points obtained from experiments; $K_{f,i}$ and $\overline{K}_{f,i}$ represent the i-th data points (the hydraulic conductivity) obtained from experiments and SFM prediction, respectively; $\boldsymbol{X}$ is the coefficient vector, which consists of the parameters listed in Table 1.

The velocity and position vectors in CPSO are expressed as (Tsoulos and Stavrakoudis, 2010):

$$v_i^{k+1} = w v_i^k + c_1 r_1 \left(p_{li}^k - x_i^k \right) + c_2 r_2 \left(p_g^k - x_i^k \right) \tag{25a}$$

$$x_i^{k+1} = x_i^k + v_i^{k+1} \tag{25b}$$

where v_i^k and x_i^k are the velocity and position of the i-th particle at the k-th iteration; w is the weight ($w < 1$); c_1 and c_2 are the cognitive and social coefficients, respectively; p_{li}^k and p_g^k represent the optimal positions encountered by the i-th particle and the entire particle swarm up to the k-th iteration; r_1 and r_2 are random numbers uniformly distributed in the range of 0–1.

Table 2
Experiment parameters in shear-seepage tests.

Sampling spot	Specimen kind	Specimen density (kg/m^3)	Specimen porosity (%)	*JRC*	*JCS* (MPa)	σ_c (MPa)	σ_t (MPa)	e_0 (mm)	σ_n (MPa)	τ_c (MPa)	ϕ_b (°)	K_{n0} (MPa/mm)	K_{s0} (MPa/mm)	Loading (mm/s)	Maximum δ_s (mm)	References
Nangen, Korea	Granite	2610	0.37	9	162	162		0.15	1, 5, 10, 20	Table 3	46.6	100	Table 3	0.1	20	Esaki et al. (1999)
Aspö, Sweden	Granite	2760		9.7	169	169	13.6		2	Table 3	31				15	Olsson and Barton (2001)
Artificial material	Pouring plaster	2066		17 and 3 (two specimens)	38.5	38.5	2.5		1, 1.5	Table 3	60			0.5	20	Xiong et al. (2011)

Remarks: (1) e_0 and K_{n0} can be calculated by Eqs. (5) and (8a) if the experimental data is insufficient; (2) A Schmidt hammer test reveals that *JCS* could be equated to σ_c (Olsson and Barton, 2001); (3) τ_c depends on the level of σ_n as shown in Table 3.

An improved version of the CPSO, referred to as the PSO-WDV method (Song et al., 2021; Xu et al., 2021), incorporates the effect of the delayed velocity into Eq. (25a):

$$v_i^{k+1} = (1-w)v_i^{k-1} + wv_i^k + c_1 r_1\left(p_{li}^k - x_i^k\right) + c_2 r_2\left(p_g^k - x_i^k\right) \tag{26}$$

where $(1-w)v_i^{k-1}$ is the weighted delay velocity term. It is a novel term that circumvents the issue of local optima, guaranteeing the attainment of the global optimum. We implement the algorithm using the PySwarms package (Miranda, 2018). The workflow of the PSO-WDV method is elaborated in Appendix A.

4. Experiment description and data source

The shear-flow experiments are conducted under diverse constant normal stresses varying within a limited range. The parameters and material properties in experiments conducted by various authors are presented in Table 2. In this study, we utilize these published experimental results to evaluate the performance of the proposed SFM.

A schematic of the testing apparatus, namely the shear box, is illustrated in Fig. 6. The normal stress σ_n is gradually increased to the designated value, then the shear displacement δ_s is applied at a specified displacement rate. In the post-processing of experimental results, the relations of hydraulic conductivity K_f versus shear displacement δ_s are obtained through back-calculation from the shear-seepage experiment.

Esaki et al. (1999) conducted a comprehensive investigation into the combined influence of shear deformation and dilatancy on hydraulic conductivity. They accomplished this by devising a novel laboratory technique for conducting shear-flow tests on rock fractures. The normal load applied in the shear-seepage process is relatively high compared to that used by other authors (up to 20 MPa). Olsson and Barton (2001) analysed the shear-seepage properties of fractures under both constant normal load and constant normal stiffness conditions. Here, for comparison with other results, we exclusively utilize the experimental data obtained under constant normal load conditions. In contrast to the natural rock (granite) utilized by Esaki et al. (1999) and Olsson and Barton (2001), Xiong et al. (2011) employed an artificial material (pouring plaster) for the test.

The hydraulic property in literature (Olsson and Barton, 2001; Xiong et al., 2011) is represented by the transmissivity T_f, which is related to K_f as follows:

$$T_f = \frac{g e_h^3}{12\nu} = K_f e_h \tag{27}$$

For comparative analysis, we convert the hydraulic conductivity K_f to the transmissivity T_f using Eq. (27) when analysing the results of Olsson and Barton (2001) and Xiong et al. (2011).

Table 3
Shear strength and initial shear stiffness in shear-seepage tests.

No.	σ_n (MPa)	τ_c (MPa)	K_{s0} (MPa/mm)	References
1	1	2.06	3.37	Esaki et al. (1999)
	5	6.16	10.65	
	10	11.74	11.97	
	20	22.1	17.97	
2	2	2.38		Olsson and Barton (2001)
3	1	0.9		Xiong et al. (2011)
	1.5	1.1		

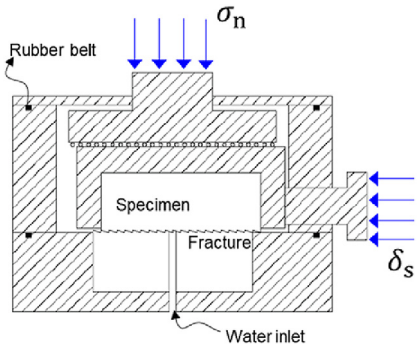

Fig. 6. Schematic of the apparatus (shear box) in the shear-seepage experiment (after Cao et al. (2018)).

5. Results and discussion

In this section, we analyse mechanical deformation and hydraulic conductivity evolution during shear-seepage. The data source used for the analysis is given in Section 4. The proposed SFM is utilized to replicate experimental results across different conditions, and to explore the impact of dilatancy and asperity on hydraulic conductivity.

5.1. Comparative analysis of different models

The model parameters in the proposed SFM are determined using the PSO-WDV method. The uncertain parameters commonly involved in both SFM-MC and SFM-*JRC* are c_f, r_f , and s_f. In SFM-Grasselli, three additional parameters are employed for exclusively capturing geometric features of the rough fracture, including A_0, θ^*_{max} and C. The values of these parameters are listed in Table 4. Obviously, their values are varied in different experiments, depending on the individual experimental apparatus and environment. Moreover, the shear strength τ_c and initial shear stiffness K_{s0} are connected to the normal stress σ_n. For this analysis, we rely on the relationships depicted in Fig. 7.

Fig. 8 displays the δ_s-u_n curves. It provides a comparison between the experimental data and the SFM results. The experimental data obtained from Esaki et al. (1999) is selected as the reference solution. The results indicate that different versions of the SFM effectively replicate the experimental outcomes across a broad spectrum of normal stresses (σ_n = 1–20 MPa). It is evident that the displacement component u_n normal to the fracture gradually diminishes as the normal stress increases. At a relatively low stress level, the maximum u_n reaches approximately 3 mm. However, at a relatively high stress level, the maximum u_n is even less than 1 mm, as depicted in Fig. 8a and d, respectively.

In another analysis, Olsson and Barton (2001) examined the shear-seepage process in a rock fracture subjected to a stress of 2 MPa. As depicted in Fig. 9, the observed trend differs from that in Esaki's experiment (Fig. 8). Specifically, the displacement u_n in Olsson's experiment demonstrates a monotonic increase under continuous shear loading, while it converges to a stable value under high stress conditions (greater than 5 MPa) in Esaki's experiment. The proposed SFM effectively captures these results with a strong alignment between the reference solutions and the predicted results.

To compare the performance of different parameter optimization methods, we utilize three distinct methods for determining model parameters, including the PSO-WDV developed in Section 3.2, the classical PSO, and the least square method (LSM). The error ε_h is defined as

Table 4
Parameters of the proposed SFM determined by the PSO-WDV method in different experiments.

SFM-MC			SFM-*JRC*			SFM-Grasselli						References
c_f	r_f	s_f	c_f	r_f	s_f	c_f	r_f	s_f	A_0	θ^*_{max} (°)	C	
0.88	0.23	0.22	0.91	0.22	0.22	0.9	0.21	0.21	0.5	80	7.6	Esaki et al. (1999)
0.96	0.18	0.11	0.89	0.19	0.11	0.95	0.3	0.12	0.49	76	7.7	Olsson and Barton (2001)
0.91	0.13	0.22	0.9	0.13	0.23	0.95	0.16	0.14	0.5	72	9.2	Xiong et al. (2011)

Note:: Other parameters can be obtained from experiments as shown in Tables 2 and 3.

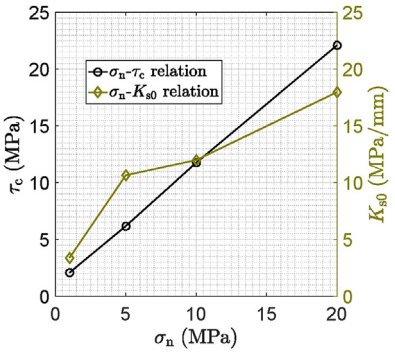

Fig. 7. Relations of σ_n-τ_c and σ_n-K_{s0} used in shear-seepage analysis (after Esaki et al. (1999)).

$$\varepsilon_h = \sum_{i=1}^{N_c} \frac{\|\Phi_i - \overline{\Phi}_i\|_2}{\|\overline{\Phi}_i\|_2} \tag{28}$$

where N_c is the number of experimental data points collected during the shear-seepage process; $\overline{\Phi}_i$ refers to the experimental data; Φ_i corresponds to the results derived from the optimization methods. Note that the maximum error among all the evaluated points is denoted as $\max(\varepsilon_h)$.

The comparison of errors obtained by different optimization methods is illustrated in Fig. 10. It is found that among these three methods, the PSO-WDV yields the smallest $\max(\varepsilon_h)$. The classical PSO exhibits relatively lower error compared to the traditional LSM, which often faces challenges related to local optima (Sun et al., 2019). Due to the incorporation of an additional delayed velocity term in the PSO-WDV, it demonstrates higher accuracy when contrasted with the classical PSO.

5.2. Hydraulic conductivity in shear-seepage process

Fig. 11 illustrates the comparison between experimental data and the SFM results. It demonstrates the efficacy of the SFM in capturing variation in the hydraulic conductivity K_f during shear-seepage. K_f gradually decreases as the normal stress increases whereas it shows an increasing trend with the progression of shear displacement. It reveals that fracture closure takes place within the range of $\delta_s \leq 5$ mm. Subsequent to this, the magnitude of K_f tends to a stable value. Note that the magnitude of the y-axis is scaled by logarithm, by the original experimental data reported in Esaki et al.

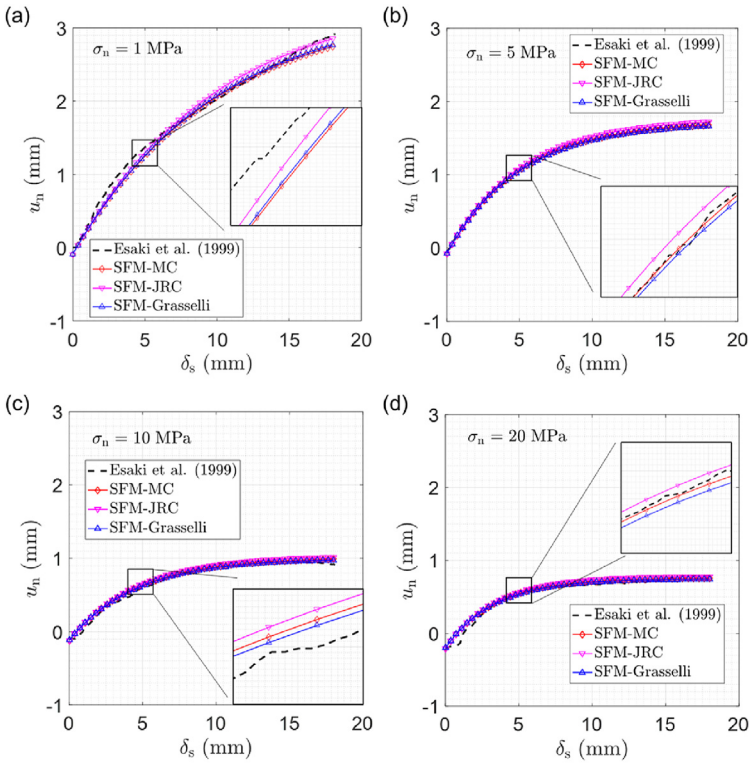

Fig. 8. Comparison of the δ_s-u_n curves obtained from experiments (Esaki et al., 1999) and various versions of the proposed SFM. The δ_s-u_n curves under different stress levels σ_n: (a) 1 MPa, (b) 5 MPa, (c) 10 MPa, and (d) 20 MPa.

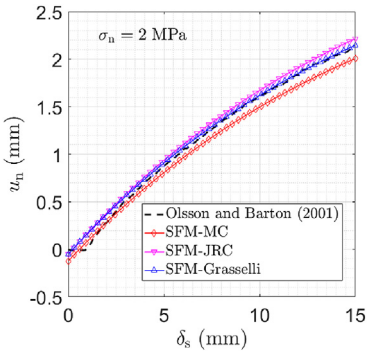

Fig. 9. Comparison of the δ_s-u_n curves obtained from experiments (Olsson and Barton, 2001) and various versions of the proposed SFM.

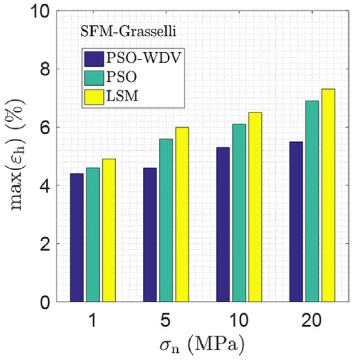

Fig. 10. The maximum error max(ε_h) of SFM-Grasselli during the shear-seepage process under different normal stresses

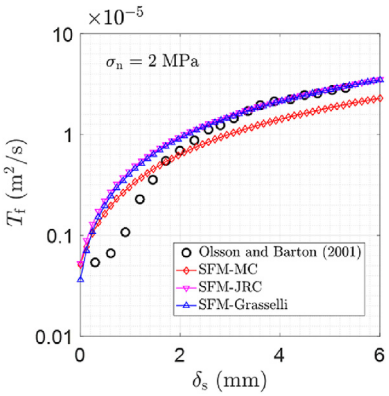

Fig. 12. Comparison of the δ_s-T_f curves obtained from experiments (Olsson and Barton, 2001) and various versions of the proposed SFM.

(1999). At a high stress level ($\sigma_n = 20$ MPa), the accuracy of the results predicted by the SFM-MC is relatively lower compared to those of the SFM-*JRC* and the SFM-Grasselli. The deviation primarily arises from the intricate mechanisms involved in the alteration of fracture asperity under high stress conditions.

A similar analysis was also conducted by Olsson and Barton (2001), but the range of shear displacement was limited to 0–6 mm, and the stress level was fixed at $\sigma_n = 2$ MPa. Note that K_f is converted to the transmissivity T_f via Eq. (27), by the original experimental data reported in Olsson and Barton (2001). The comparative results are displayed in Fig. 12. The results obtained from the SFM-Grasselli and SFM-*JRC* models exhibit a remarkable consistency, closely aligning with the experimental data. Model parameters (c_f, r_f , and s_f) obtained from different optimization methods are shown in Fig. 13. The range of all these parameters is limited within 0–1.

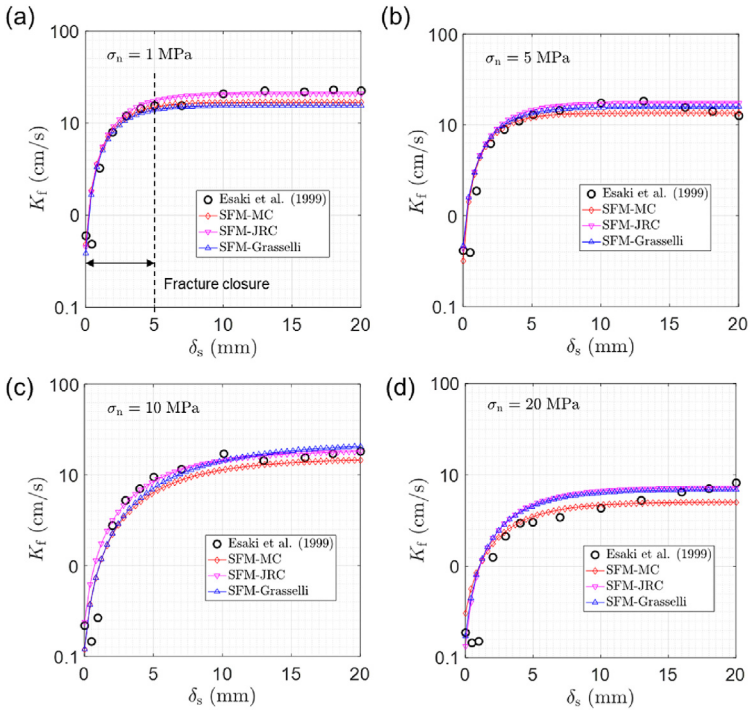

Fig. 11. Comparison of the δ_s-K_f curves obtained from experiments (Esaki et al., 1999) and various versions of the proposed SFM. The δ_s-K_f curves under different stress levels σ_n: (a) 1 MPa, (b) 5 MPa, (c) 10 MPa, and (d) 20 MPa.

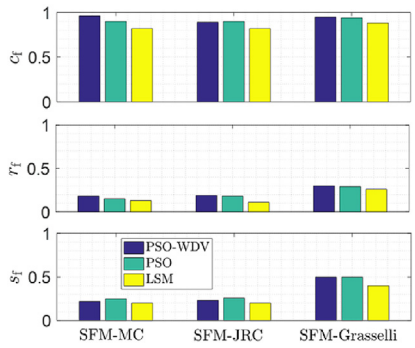

Fig. 13. Coefficients used in the proposed SFM obtained by different optimization methods in the Olsson-Barton experiment (Figs. 9 and 12).

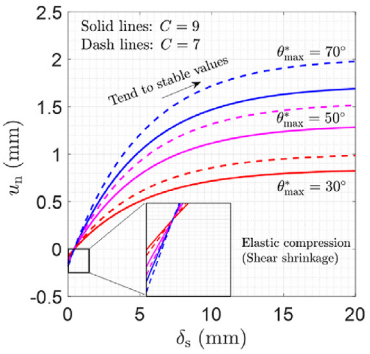

Fig. 17. Variation of the displacement component u_n normal to the fracture with different asperity parameters during the shear-seepage process.

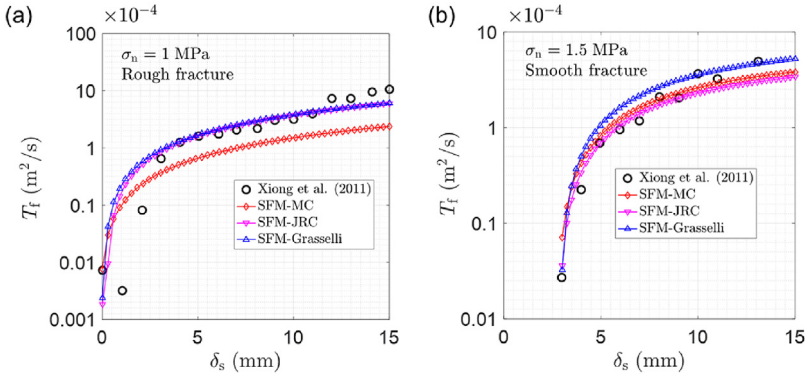

Fig. 14. Comparison of the δ_s-T_f curves obtained from experiments (Xiong et al., 2011) and various versions of the proposed SFM. The δ_s-T_f curves under different conditions: (a) Rough fracture with $\sigma_n = 1$ MPa, and (b) Smooth fracture with $\sigma_n = 1.5$ MPa.

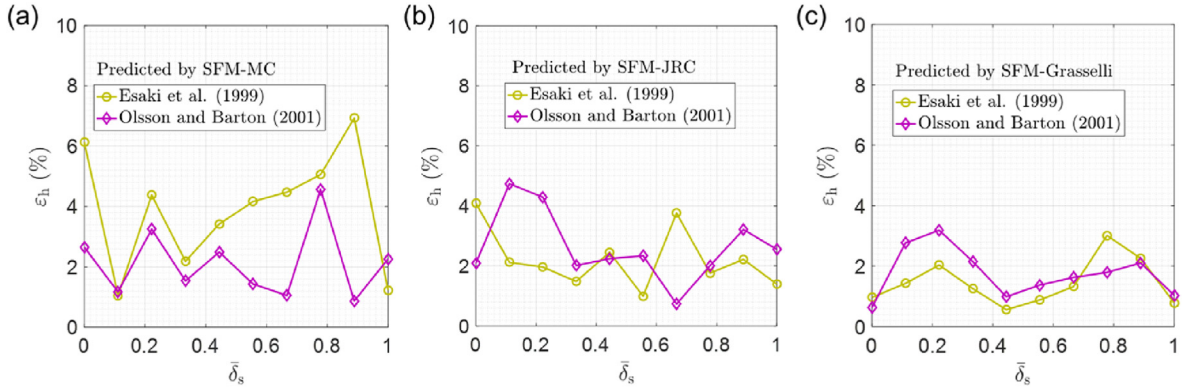

Fig. 15. Variation of error ε_h predicted by different versions of the proposed SFM: (a) SFM-MC, (b) SFM-*JRC*, and (c) SFM-Grasselli.

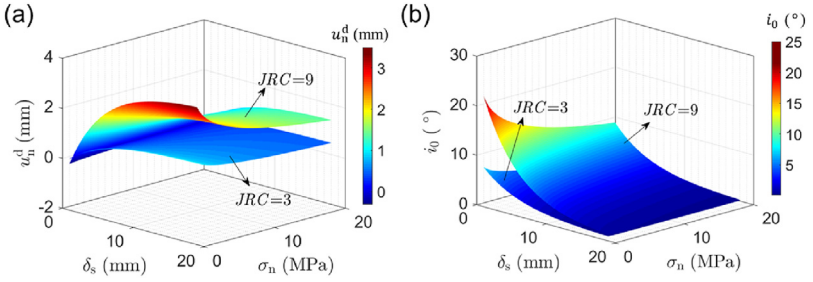

Fig. 16. Variations of dilatancy-induced deformation u_n^d and dilatancy angle i_0 under different conditions during the shear-seepage process: (a) The effect of σ_n and δ_s on u_n^d, and (b) The effect of σ_n and δ_s on i_0.

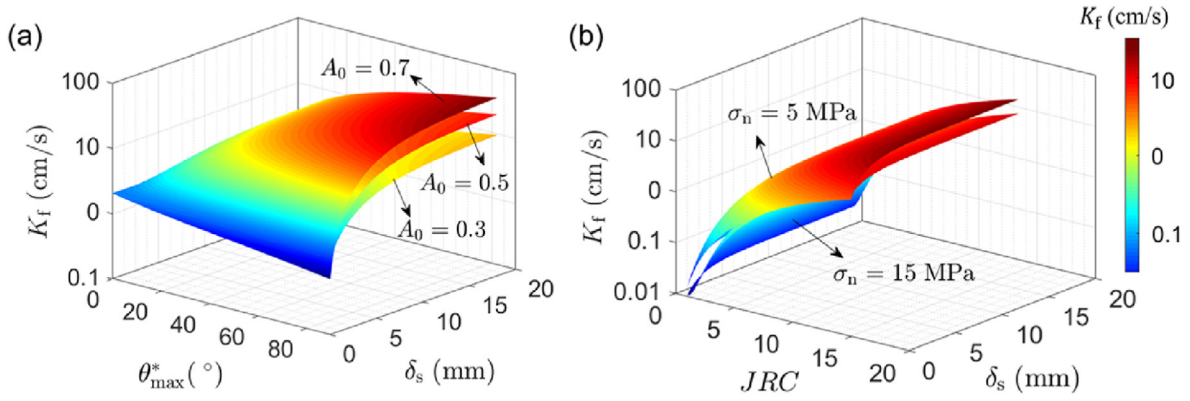

Fig. 18. Variation of hydraulic conductivity K_f under different conditions: (a) The effect of fracture asperity (measured by θ^*_{max} and A_0) on K_f, and (b) The effect of *JRC* and stress σ_n on K_f.

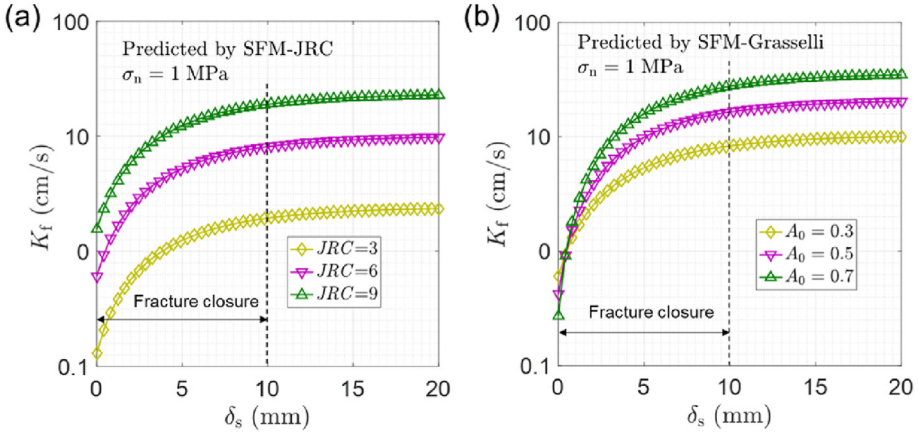

Fig. 19. Effect of fracture asperity (measured by *JRC* and A_0) on hydraulic conductivity K_f under a constant stress ($\sigma_n = 1$ MPa): (a) Predicted by SFM-*JRC*, and (b) Predicted by SFM-Grasselli.

Fig. 14 illustrates the results of rough fracture and smooth fracture (Xiong et al., 2011). For a rough fracture, the accuracy of the SFM-MC is lower than that of the other two models, since the SFM-MC cannot exclusively describe fracture roughness. The comparative results demonstrate that the SFM-*JRC* and the SFM-Grasselli are able to satisfactorily capture the variation of hydraulic property in both the rough and smooth fractures. In the case of smooth fractures, the SFM-Grasselli demonstrates superior performance, but it requires more additional parameters (A_0, θ^*_{max} and C) than other models, as indicated in Table 4.

The disparity between the predicted results and the experimental data dynamically changes throughout the shear-seepage process. We compute the error ε_h using Eq. (28), where the experimental results are considered as the reference solutions. For comparison, the x-axis is scaled by a normalized shear displacement, denoted as $\bar{\delta}_s = \delta_s/\max(\delta_s)$. The observation shown in Fig. 15 reveals that the error varies throughout the shearing process, exhibiting distinct patterns in different shear-seepage processes. Although the error magnitude exhibits a random nature, it remains relatively small in SFM-Grasselli. In contrast, SFM-MC results in a comparatively significant deviation.

5.3. Effect of dilatancy and asperity

As discussed in the preceding sections, the asperities on the rock fracture induce the dilatancy-induced deformation u^d_n. The dilatancy effect is intricately associated with variations in the dilatancy angle i_0. In the SFM-*JRC*, the parameter *JRC* serves as an indicator of fracture roughness. Fig. 16a depicts a three-dimensional (3D) surface depicting the evolution of u^d_n with changes in shear displacement δ_s and normal stress σ_n. It illustrates that the dilatancy effect becomes pronounced as shearing progresses but diminishes with increasing stress levels. Moreover, the increase of *JRC* substantially amplifies the dilatancy effect. The dilatancy u^d_n tends to a stable value after a certain shear displacement. The dilatancy angle i_0 exhibits a contrasting pattern when compared to that of u^d_n, as illustrated in Fig. 16b. As shear displacement increases, there is a gradual decrease in the value of i_0. This observation reflects a fact that the fracture asperities undergo abrasion due to local shear failure.

The SFM-Grasselli provides numerous parameters for characterizing the geometric features of fracture asperity. Specifically, the maximum apparent dip angle θ^*_{max} signifies the inclination degree of these asperities, as defined in Eq. (20). Fig. 17 illustrates variation of the displacement u_n normal to the fracture with different θ^*_{max}. Obviously, the increase of θ^*_{max} improves the magnitude of normal displacement. It is evident that the steeper the dip angle, the greater the effect. This also implies that the dilatancy effect will vanish if θ^*_{max} is set to zero. Notably, a shear shrinkage effect is observed at the onset of shear loading, which can be attributed to the elastic deformation of asperities under compressive loading (Cao et al., 2018).

To further analyse the effect of fracture asperities, we investigate the evolution of hydraulic conductivity K_f under varying conditions. To achieve this, we conduct a sensitivity analysis involving different asperity parameters. The characteristic of asperities in the SFM-Grasselli is represented by A_0 and θ^*_{max}, whereas in the SFM-*JRC*, it is captured by *JRC*. The maximum contact area A_0 serves as an indicator of the contact state of rock fracture. Fig. 18a shows that an increase in A_0 corresponds to a rise in K_f. The influence of θ^*_{max} becomes more pronounced at a higher δ_s, eventually stabilizing once a certain δ_s threshold is attained. Fig. 18b shows that K_f decreases at a high σ_n level, which is attributed to the decrease in fracture aperture caused by fracture closure under compression. A more comprehensive result can be found in Fig. 19. Fracture closure takes place within the range of $\delta_s \leq$ 10 mm, after which K_f tends to stabilize. Under a constant normal stress condition (1 MPa), increasing both *JRC* and A_0 improves the magnitude of K_f, attributed to the increased fracture asperities.

6. Conclusions and outlook

In this work, we investigate the hydro-mechanical characteristics of rough rock fracture during shear-seepage process. The main concluding remarks and implications are summarized as follows:

(1) The improved shear-flow model (SFM) consists of stress-dependent hydraulic conductivity, fracture closure, and asperity-induced dilatancy effect. In particular, shear dilatancy is considered in both the elastic and plastic stages. The SFM-*JRC*, SFM-MC, and SFM-Grasselli are presented based on different computation approaches of the peak dilatancy angle. Notably, although Grasselli's model has been applied in shear strength analysis, it is rarely utilized in the shear-seepage process.

(2) The PSO-WDV method is introduced to accurately identify parameters involved in the SFM. It incorporates the delayed velocity term and addresses the issue of local optima in classical methods. Numerous tests demonstrate the superiority of PSO-WDV, showing the capacity to enhance the accuracy of parameter determination.

(3) By comparing with experimental data, the results show that the SFM is capable of reproducing the shear-seepage characteristics across a wide range of stress levels (from 1MPa to 20 MPa). The SFM-Grasselli performs well, although it requires more parameters than the SFM-MC and SFM-*JRC*. The SFM-MC shows relatively lower accuracy when applied to predict hydraulic conductivity under a high stress state (20 MPa).

(4) Sensitivity analysis reveals the effect of dilatancy and asperity on shear-seepage. We analyse the relation between hydro-mechanical properties and the asperity parameters. The dilatancy effect depends on the variation in the dilatancy angle. This effect becomes more pronounced as shearing progresses but gradually decreases at higher stresses. An underlying fact is that the asperities undergo abrasion due to local shear failure. The shear shrinkage effect is observed at the onset of shearing, attributed to the elastic deformation of asperities under compressive loading.

Ongoing research aims to adapt the proposed model for geotechnical application. We intend to integrate it into our program for simulating flow in fractured media (Wang et al., 2022a, b, c).

Declaration of competing interest

The authors declare that they have no known competing financial interests or personal relationships that could have appeared to influence the work reported in this paper.

Acknowledgments

We acknowledge the funding support from the National Natural Science Foundation of China (Grant Nos. 51991392 and 42293355).

Appendix A. Supplementary data

Supplementary data to this article can be found online at https://doi.org/10.1016/j.jrmge.2023.11.020.

References

Barton, N., Bandis, S., 1980. Some effects of scale on the shear strength of joints. Int. J. Rock Mech. Min. Sci. 17 (1), 69–73.
Barton, N., Bandis, S., 1982. Effects of block size on the shear behaviour of jointed rocks. In: Proceedings of the 23rd US Symposium on Rock Mechanic, pp. 739–760. Berkeley, USA.
Barton, N., Bandis, S., Bakhtar, K., 1985. Strength, deformation and conductivity coupling of rock joints. Int. J. Rock Mech. Min. Sci. 22 (3), 121–140.
Barton, N., 2014. Non-linear behaviour for naturally fractured carbonates and frac-stimulated gas-shales. First Break 32 (9), 51–66.
Barton, N., Wang, C., Yong, R., 2023. Advances in joint roughness coefficient (JRC) and its engineering applications. J. Rock Mech. Geotech. Eng. 15 (12), 3352–3379.
Bisdom, K., Bertotti, G., Nick, H.M., 2016. The impact of different aperture distribution models and critical stress criteria on equivalent permeability in fractured rocks. J. Geophys. Res. Solid Earth 121 (5), 4045–4063.
Cao, C., Xu, Z., Chai, J., Qin, Y., Tan, R., 2018. Mechanical and hydraulic behaviors in a single fracture with asperities crushed during shear. Int. J. GeoMech. 18 (11), 04018148.
Chen, Y., Zhou, C., Sheng, Y., 2007. Formulation of strain-dependent hydraulic conductivity for a fractured rock mass. Int. J. Rock Mech. Min. Sci. 44, 981–996.
Chen, W., Sui, Q., Wang, L., Xie, P., Tian, Y., 2021a. Development and application of a hydro-mechanical coupling shear creep testing machine for rock joints. Chinese J. Rock Mech. Eng. 9, 1729–1738 (in Chinese).
Chen, W., Wang, L., Tan, X., Yang, D., Yuan, J., Yang, J., 2021b. State-of-the-art and development tendency of the underground engineering stability of fractured rock mass. Chinese J. Rock Mech. Eng. 10, 945–1961 (in Chinese).
Cunningham, D., Auradou, H., Shojaei-Zadeh, S., Drazer, G., 2020. The effect of fracture roughness on the onset of nonlinear flow. Water Resour. Res. 56 (11), e2020WR028049.
Dietrich, P., Helmig, R., Sauter, M., Teutsch, G., Hötzl, H., Köngeter, J., 2005. Flow and Transport in Fractured Porous Media. Springer-Verlag Berlin Heidelberg, Germany.
Esaki, T., Du, S., Mitani, Y., Ikusada, K., Jing, L., 1999. Development of a shear-flow test apparatus and determination of coupled properties for a single rock joint. Int. J. Rock Mech. Min. Sci. 36, 641–650.
Gan, L., Liu, Y., Xu, T., Xu, L., Ma, H., Xu, W., 2023. Experimental investigation of the seepage characteristics of a single fracture in limestone with different roughness and seepage fluids. J. Hydrol. 622, 129699.
Grasselli, G., Wirth, J., Egger, P., 2002. Quantitative three-dimensional description of a rough surface and parameter evolution with shearing. Int. J. Rock Mech. Min. Sci. 39 (6), 789–800.
Grasselli, G., Egger, P., 2003. Constitutive law for the shear strength of rock joints based on three-dimensional surface parameters. Int. J. Rock Mech. Min. Sci. 40 (1), 25–40.
Hudson, J.A., Stephansson, O., Andersson, J., Tsang, C.F., Jing, L., 2001. Coupled THM issues relating to radioactive waste repository design and performance. Int. J. Rock Mech. Min. Sci. 38 (1), 143–161.
Jaeger, J.C., Cook, N.G., Zimmerman, R., 2009. Fundamentals of Rock Mechanics. Blackwell Publishing, Oxford, UK.
Jiang, Y., Li, B., Wang, C., Song, Z., Yan, B., 2022. Advances in development of shear-flow testing apparatuses and methods for rock fractures: a review. Rock Mech. Bull. 1 (1), 100005.
Kim, D.H., Gratchev, I., Balasubramaniam, A., 2013. Determination of joint roughness coefficient (JRC) for slope stability analysis: a case study from the Gold Coast area, Australia. Landslides 10, 657–664.
Kolditz, O., Görke, U.J., Shao, H., Wang, W., 2012. Thermo-hydro-mechanical-chemical Processes in Fractured Porous Media. Springer-Verlag Berlin Heidelberg, Germany.
Lee, H.S., Cho, T.F., 2002. Hydraulic characteristics of rough fractures in linear flow under normal and shear load. Rock Mech. Rock Eng. 35 (4), 299–318.

Li, Z., Ma, X., Kong, X.Z., Saar, M.O., Vogler, D., 2023. Permeability evolution during pressure-controlled shear slip in saw-cut and natural granite fractures. Rock Mech. Bull. 2 (2), 100027.
Liu, Q., Tian, Y., Liu, D., Jiang, Y., 2017. Updates to JRC-JCS model for estimating the peak shear strength of rock joints based on quantified surface description. Eng. Geol. 228, 282–300.
Liu, R., Lou, S., Li, X., Han, G., Jiang, Y., 2020. Anisotropic surface roughness and shear behaviors of rough-walled plaster joints under constant normal load and constant normal stiffness conditions. J. Rock Mech. Geotech. Eng. 12 (2), 338–352.
Liu, J., Qiu, X., Yang, J., Liang, C., Dai, J., Bian, Y., 2023. Failure transition of shear-to-dilation band of rock salt under triaxial stresses. J. Rock Mech. Geotech. Eng. 11 (2), 56–64.
Louis, C., 1974. Introduction a l'hydraulique des roches. PhD Thesis. Bureau Recherches Geologique Miniers. Orleans, France.
Matsuki, K., Lee, J.J., Sakaguchi, K., Hayashi, K., 1999. Size effect in flow conductance of a closed small-scale hydraulic fracture in granite. Geotherm. Sci. Tech. 6 (1–4), 113–138.
Miranda, L.J., 2018. PySwarms: a research toolkit for particle swarm optimization in Python. J. Open Source Softw. 3 (21), 433.
Olsson, R., Barton, N., 2001. An improved model for hydromechanical coupling during shearing of rock joints. Int. J. Rock Mech. Min. Sci. 38, 317–329.
Rasouli, V., Hosseinian, A., 2011. Correlations developed for estimation of hydraulic parameters of rough fractures through the simulation of JRC flow channels. Rock Mech. Rock Eng. 44, 447–461.
Sawayama, K., Ishibashi, T., Jiang, F., Tsuji, T., Fujimitsu, Y., 2021. Relating hydraulic-electrical-elastic properties of natural rock fractures at elevated stress and associated transient changes of fracture flow. Rock Mech. Rock Eng. 54, 2145–2164.
Segall, P., Simpson, C., 1986. Nucleation of ductile shear zones on dilatant fractures. Geology 14 (1), 56–59.
Song, B., Wang, Z., Zou, L., 2021. An improved PSO algorithm for smooth path planning of mobile robots using continuous high-degree Bezier curve. Appl. Soft Comput. 100, 106960.
Sui, Q., Chen, W., Wang, L., 2022. Investigation of nonlinear flow in discrete fracture networks using an improved hydro-mechanical coupling model. Appl. Sci. 12, 3027.
Sun, S., Cao, Z., Zhu, H., Zhao, J., 2019. A survey of optimization methods from a machine learning perspective. IEEE Trans. Cybern. 50 (8), 3668–3681.
Tan, X., Chen, W., Wang, L., Yang, J., Tan, X.J., 2021. Settlement behaviors investigation for underwater tunnel considering the impacts of fractured medium and water pressure. Mar. Geores. Geotechnol. 39, 639–648.
Tan, X., Chen, W., Wang, L., Qin, C., 2023. Spatial deduction of mining-induced stress redistribution using an optimized non-negative matrix factorization model. J. Rock Mech. Geotech. Eng. 15 (11), 2868–2876.
Tang, Z.C., Zhang, Z.F., Zuo, C.Q., Jiao, Y.Y., 2021. Peak shear strength criterion for mismatched rock joints: Revisiting JRC-JMC criterion. Int. J. Rock Mech. Min. Sci. 147, 104894.
Tatone, B.S., Grasselli, G., 2009. A method to evaluate the three dimensional roughness of fracture surfaces in brittle geomaterials. Rev. Sci. Instrum. 80 (12), 181-106.
Thompson, M.E., Brown, S.R., 1991. The effect of anisotropic surface roughness on flow and transport in fractures. J. Geophys. Res. Solid Earth 96 (B13), 21923–21932.
Tsoulos, I.G., Stavrakoudis, A., 2010. Enhancing PSO methods for global optimization. Appl. Math. Comput. 216 (10), 2988–3001.
Wang, L., Chen, W., Tan, X.Y., et al., 2020. Numerical investigation on the stability of deforming fractured rocks using discrete fracture networks: a case study of underground excavation. Bull. Eng. Geol. Environ. 79, 133–151.
Wang, L., Golfier, F., Tinet, A.J., Chen, W., Vuik, C., 2022a. An efficient adaptive implicit scheme with equivalent continuum approach for two-phase flow in fractured vuggy porous media. Adv. Water Resour. 163, 104186.
Wang, L.Y., Chen, W.Z., Zhang, Y.J., Zhang, X.D., Vuik, C., 2022b. Investigating Effects of Heterogeneity and Fracture Distribution on Two-phase Flow in Fractured Reservoir with Adaptive Time Strategy. Transp. Porous Media, pp. 1–29.
Wang, L., Wang, Y., Vuik, C., Hajibeygi, H., 2022c. Accurate modeling and simulation of seepage in 3D heterogeneous fractured porous media with complex structures. Comput. Geotech. 150, 104923.
Witherspoon, P.A., Wang, J.S., Iwai, K., Gale, J.E., 1980. Validity of cubic law for fluid flow in a deformable rock fracture. Water Resour. Res. 16 (6), 1016–1024.
Xia, C.C., Tang, Z.C., Xiao, W.M., Song, Y.L., 2014. New peak shear strength criterion of rock joints based on quantified surface description. Rock Mech. Rock Eng. 47 (2), 387–400.
Xiong, X., Li, B., Jiang, Y., Koyama, T., Zhang, C., 2011. Experimental and numerical study of the geometrical and hydraulic characteristics of a single rock fracture during shear. Int. J. Rock Mech. Min. Sci. 48, 1292–1302.
Xu, L., Song, B., Cao, M., 2021. An improved particle swarm optimization algorithm with adaptive weighted delay velocity. Syst. Sci. Control Eng. 9 (1), 188–197.
Zhang, Y., Zou, Y., Zhang, Y., et al., 2022a. Experimental study on characteristics and mechanisms of matrix pressure transmission near the fracture surface during post-fracturing shut-in in tight oil reservoirs. J. Pet. Sci. Eng. 219, 111133.
Zhang, Y., Ye, J., Li, P., 2022b. Flow characteristics in a 3D-printed rough fracture. Rock Mech. Rock Eng. 55 (7), 4329–4349.
Zhou, C.B., Chen, Y.F., Hu, R., Yang, Z., 2023. Groundwater flow through fractured rocks and seepage control in geotechnical engineering: theories and practices. J. Rock Mech. Geotech. Eng. 15 (1), 1–36.

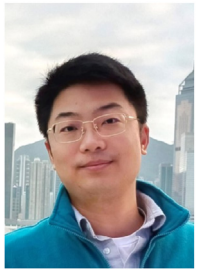

Dr. Luyu Wang obtained his BSc degree in mining engineering from Shandong University of Science and Technology, China, in 2015, and his PhD degree in geotechnical engineering at Institute of Rock and Soil Mechanics, Chinese Academy of Sciences, China, in 2021. He is now a postdoctoral fellow at The Hong Kong Polytechnic University (PolyU), Hong Kong, China. Before joining PolyU, he was a visiting PhD student at Delft University of Technology, The Netherlands, and later continued his career as a postdoctoral fellow at CNRS-GeoRessources Lab., France. He is a member of the Youth Editorial Board for two international journals and serves as a guest editor for a special issue in an SCI-indexed journal. His research interests include damage and fracture of geomaterials, flow and transport in 3D fractured media, and stress-seepage coupling in rocks.